HENRY GRANJON PRIZE COMPETITION 2004
Winner, Category A
"Joining and fabrication technology"

MODELLING AND DEVELOPMENT OF THE TRIVEX™ FRICTION STIR WELDING TOOL

P.A. Colegrove
Cambridge University (United Kingdom)
E-mail: pac44@cam.ac.uk

ABSTRACT

This work has demonstrated the development and benefits of the Trivex™ tool over the conventional MX-Triflute™ tool in friction stir welding of aluminium alloys. This tool was developed from 2 dimensional models. Experiments made on 7075-T7351 aluminium alloy verified this result. Three dimensional thermal models that used the experimental heat input predicted the weld thermal profile, which correlated well with the experimental curves. The work also demonstrated several novel modelling techniques. The first was the slip boundary condition in 3 dimensions, where a limiting shear stress was applied at the surface and the material was allowed to slip against the tool. The second involved adjusting the limiting shear stress so that the weld power of the model matched that obtained experimentally. The final technique was the inclusion of the temperature profile by interpolating the result from a thermal model. This obviated the need to solve the thermal profile in conjunction with the flow model.

IIW-Thesaurus keywords: *Friction stir welding; Friction welding; Mathematical models; Aluminium alloys; Light metals; Optimisation; Tools; Comparisons; Influencing factors; Practical investigations; Thermomechanically affected zone; Weld zone; Welded joints; Reference lists.*

1 INTRODUCTION

Friction stir welding (FSW) is a relatively new welding process, patented in 1991 by Thomas *et al*. [1, 2]. This process has great advantages in welding aluminium alloys that are difficult to weld. The process gives low distortion, can weld thick sections in a single pass and produces welds with excellent mechanical properties.

A schematic diagram illustrating the process of FSW is shown in Figure 1. The key components of the FSW tool are:

- The Shoulder. This is the primary means of generating heat during the process, it prevents material expulsion and assists material movement around the tool.
- The Pin. The pin's primary function is to deform the material around the tool and its secondary function is to generate heat.

Modelling of friction stir welding (FSW) has been reviewed by Shercliff and Colegrove [3]. Friction stir models to date have focussed on thermal field prediction, with some studies leading to the prediction of microstructural evolution, properties and residual stress. Because the flow around the tool is largely rotational, a good first estimate of the flow can be obtained with a 2 dimensional flow model of the pin. Xu *et al*. [4], Seidel and Reynolds [5] and Colegrove and Shercliff [6] have demonstrated how 2 dimensional models can be used to visualise the flow. Three dimensional flow modelling of threaded tools has been attempted by Askari *et al*. [13], Bendzsak *et al*. [14] and Colegrove *et al*. [11, 16] and cylindrical tools have been modelled by Goetz and

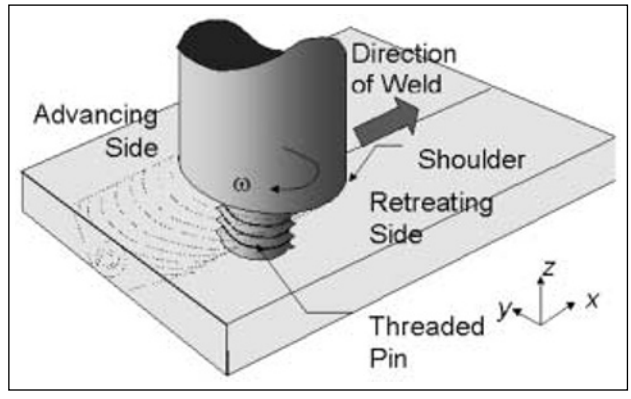

Fig. 1. Schematic diagram of friction stir welding.

Doc. IIW-1647-04 (ex-doc. III-1289-04) recommended by publication by Commission III "Resistance welding, solid state welding and allied joining processes".

Jata [17], Dong *et al*. [18] and Ulysse [19] and Xu and Deng [4]. While some impressive flow visualisation work has been demonstrated [13, 14, 4] none of these analyses have demonstrated how different tool profiles can be compared.

Xu *et al*. [4] examined the effect of slip in 2 dimensional flow around a cylindrical pin. Colegrove and Shercliff [6] extended this concept to profiled tools and assumed that the shear stress was limited to some arbitrary value. In these models two different boundary conditions could exist simultaneously on different parts of the pin:

a) Stick condition: this occurred where the shear stress was below a limiting shear stress. On a profiled tool this usually occurred in the tool flutes.

b) Slip condition: where the shear stress necessary for a stick condition exceeded the limiting value, the applied shear stress was truncated to a limiting value, which resulted in the material slipping across the tool surface.

This work uses this technique to optimise a 2 dimensional pin profile. In particular, the profile that minimises the traversing force while maintaining the rotational torque was selected.

2 OPTIMISATION OF THE 2D PROFILE

2.1 Description of the model

The two dimensional model used the Computational Fluid Dynamics (CFD) package, FLUENT [7] and is identical to the one reported in Colegrove and Shercliff [6]. This model used 7075-T6 aluminium alloy, and assumed an isothermal temperature of 527 °C. The material property of most interest is the viscosity, which was interpolated from experimental stress vs. strain-rate data produced by Jin *et al*. [8] and implemented in FLUENT through user-defined code. A rotation speed of 250 rpm and a welding speed of 300 mm/min were used for all the models. Each of the tools were examined with a stick boundary condition, and slip boundary conditions where the shear stress was limited to 80 MPa, 40 MPa or 20 MPa. These values enabled a sensitivity analysis to be conducted and are the right order of magnitude for the temperature and strain-rate conditions that exist when friction stir welding 7075-T6.

All the models analysed are steady-state where the solution is a 'snap-shot' of the flow at a particular instant in time. Provided the time-dependent terms in the Navier-Stokes equation remain relatively small, this approximation will be reasonable. The force results reported are for a single tool orientation. The effect of tool orientation has been analysed in Colegrove and Shercliff [6] and shown to be small, in terms of net forces and torque (as is observed experimentally).

The profiles used for the comparison are shown in Figure 2. All tool shapes had a cross sectional area of 121 mm^2 and a tool area to swept area ratio of 80.7%. The one exception is Tool_6 where the tool area to swept area ratio is obviously 1. The first three profiles compare the effect of flat (Tool_1), concave (Tool_2) and convex (Tool_3) features on the tool. Tool_4 combines the convex features from (Tool_2) while retaining part of the cylindrical section of the tool. Finally, Tool_5 examines convex features on a 4 sided tool.

2.2 Results

The torque results are shown in Figure 3a and the traversing force results are shown in Figure 3b. As the analysis is 2 dimensional, all forces and torques are expressed per metre of tool in the out of plane direction. There is very little difference in the torque readings for the five profiled tool shapes. As expected, the cylindri-

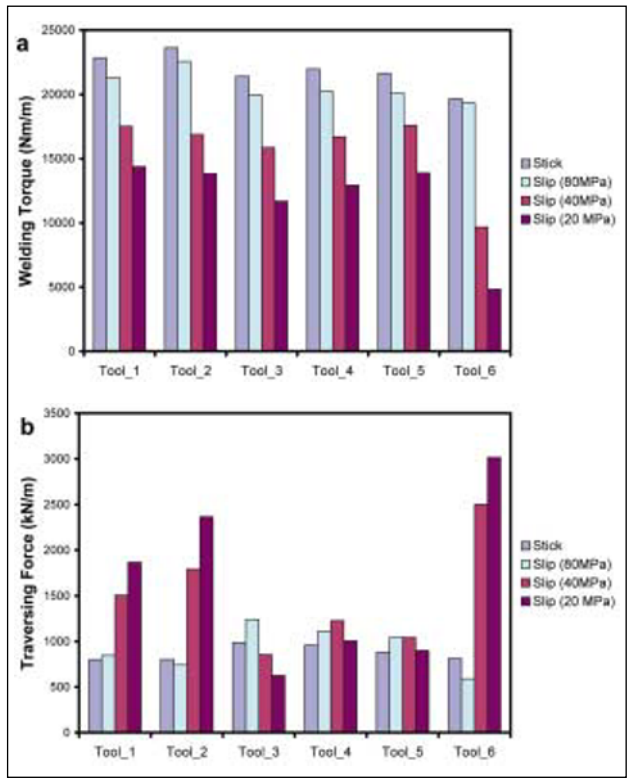

Fig. 3. Comparison between the predicted values of: (a) welding torque, (b) traversing force, for the six tool profiles.

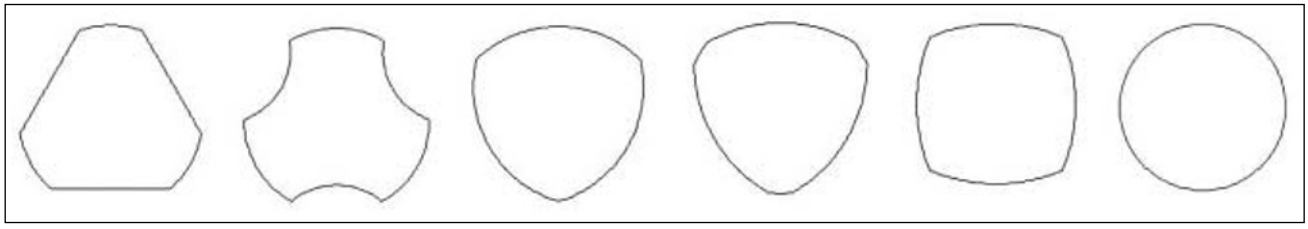

Fig. 2. Tool profiles examined.

cal shape had the lowest values because there are no features to impede the flow of the slipping material. Of the profiled tools, Tool_3 had slightly lower torque readings, which was likely to be a consequence of the convex features of this tool shape.

The results for the traversing force show much greater variability. For the tools without convex features the following approximate relationship holds:

(Limiting shear stress) α (Welding torque)
α 1/(Traversing force) (1)

This makes intuitive sense in that the greater the welding torque that can be applied to the material, the more effective the stirring action and the lower the traversing force. However, in the case of the convex tools and Tool_3 in particular the opposite is the case. i.e.

(Limiting shear stress) α (Welding torque)
α (Traversing force) (2)

This result is discussed in the following section.

3 TOOL CROSS SECTION OPTIMISATION

3.1 Model types

This section analyses the variation in welding torque and traversing force with the ratio of tool area to swept area. Tool_1 and Tool_3 were chosen for this analysis, because of the practical interest in these shapes. Note that each tool can be regarded as lying between the two extreme profiles of a circle and a triangle. For Tool_1, the ratio of tool area to swept area was varied between the limits of a circle and a triangle by adjusting the distance of the flats from the tool centre. For the Trivex™ concept (Tool_3), the critical dimensions and areas could be related via the tool geometry (Figure 4a). For given a and R_a, R_b is found from the following relationship:

$$R_b = \sqrt{a^2 + R_a^2 + aR_a} \quad (3)$$

The cross sectional area is given by:

$$A = 3R_b^2 \sin^{-1}\left(\frac{\sqrt{3R_a}}{2R_b}\right) - \frac{3\sqrt{3}}{2} aR_a \quad (4)$$

The relationship between the offset distance, a (normalised with radius R_a) and the ratio of tool area to swept area ratio is shown in Figure 4b.

3.2 Results and discussion

Figures 5a and 5b show the torque and force results for the range of area ratios between a circle and triangle for Tool_1. The results hold to the "intuitive" relationship in equation (1) across all values of the tool area to swept area ratio, R. Interestingly the curves for the different models converged when the shape became a triangle. This shape required very little shear stress for the material to stick to the profile so each of the slip models were equivalent.

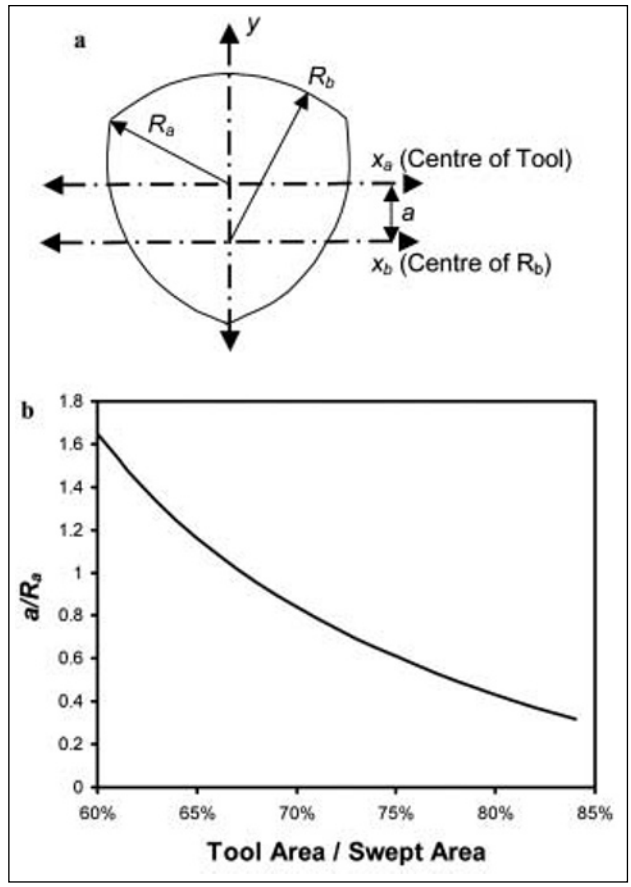

Fig. 4. (a) Critical dimensions for the Trivex™ profile (b) Variation in a/R_a with tool area to swept area ratio.

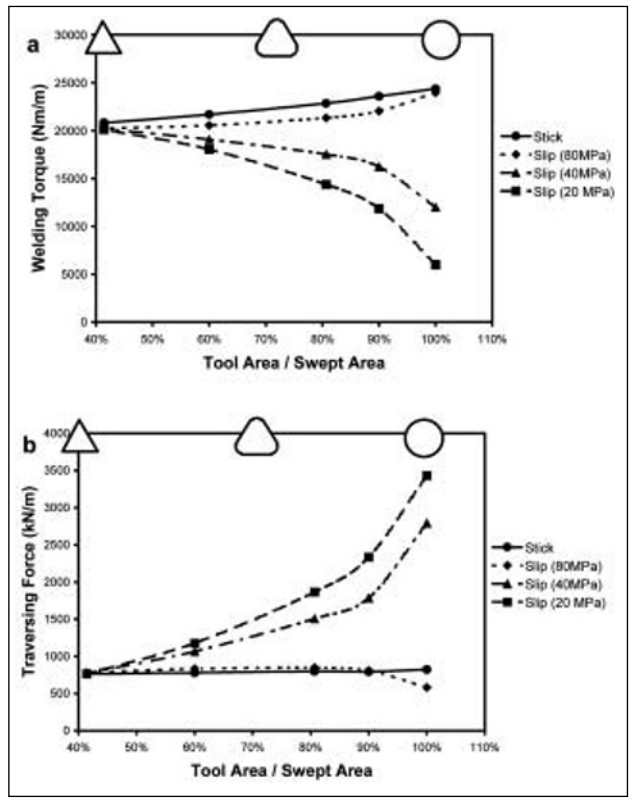

Fig. 5. Predicted variation in (a) welding torque for Tool_1; (b) traversing force for Tool_1

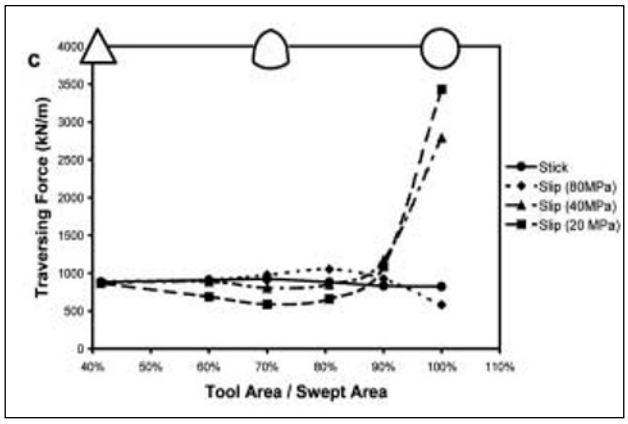

Fig. 5. Predicted variation in (c) traversing force for Tool_3 with tool area to swept area ratio.

There is a large difference between the different model types for the cylindrical tool shape. Interestingly, this shape had a greater welding torque and a slightly lower welding force than its profiled counterparts for material that is sticking to the tool (Stick model and Slip (80 MPa)). This result suggests that this shape may be more effective than profiled tooling for welding materials that tend to stick to the tool surface.

A plot of the welding torque for Tool_3 is not shown but is very similar to that shown in Figure 5a for Tool_1. The traversing force for Tool_3 is shown in Figure 5c and is substantially different to the same plot for Tool_1 in Figure 5b. Figure 5c demonstrates how the traversing force "flattens out" and is fairly insensitive to the limiting shear stress when *R* is lower than 90%. Indeed, the traversing force is minimised when *R* is between 70-80% for the 20 and 40 MPa slip models. Tests showed that this result was independent of the tool orientation, welding speed, rotation speed and the size of the tool. It should be remembered that the larger the tool area the stronger the tool and the less susceptible it will be to breakage.

A theory explaining the cause of the different traversing force characteristics is as follows: The traversing force exerted on a tool profile is a consequence of two effects:

a) The amount of stirring that the profile induces around the tool. The greater the stirring the lower the force required to push the tool through the welded material.

b) The degree to which material is trapped in the features of the profile. It appears that where the features of the tool entrap material this actually increases the traversing force. This effect will be particularly significant on the advancing side where shearing occurs within the trapped material, which is moving in an opposite direction to the flow. This increases the force in the welding direction. A profile that enables material to "flow" or slip across the tool surface avoids this large shearing force effect, lowering the traversing force.

As a consequence the convex tools that promote material slip while maintaining the tool's ability to stir the material minimise the traversing force.

4 EXPERIMENTAL VALIDATION OF THE TRIVEX™ TOOL CONCEPT

4.1 Tool design and experimental work

Two tools based on the Trivex™ concept were produced and are shown in Figure 6. The first tool (a) had no threads while the second (b) was threaded along the length. It was thought that the threads on the second tool would aid oxide disruption leading to a stronger joint. These two tools were then compared against one based on the MX-Triflute™ concept [9, 10] with the same pin and shoulder dimensions. It was difficult to make the two tools identical in every respect, which is demonstrated by the comparison of moments of inertia and tool area to swept area ratios in Table 1.

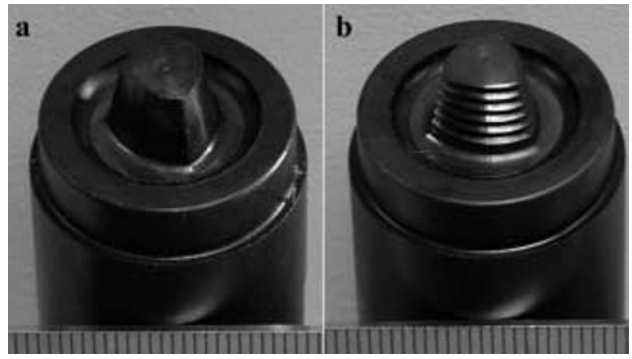

Fig. 6. (a) Trivex™ and (b) MX-Trivex™ tools.

Welds were made using 6.35 mm 7075-T7351 aluminium alloy using the ESAB SuperStir™ machine at TWI (Cambridge, UK). The welding conditions used are summarised in Table 2. This machine permitted the measurement of traversing and down forces as well as the welding torque. Thermocouples were placed in the material at the locations shown in Figure 7 to measure the weld temperature. Thermocouples were also placed along the centreline, however the weld temperature of 500 °C exceeded the 400 °C limit of these thermocouples. Because the welding temperature for MX-Triflute™ welds in 6.35 mm 7075 aluminium has already been extensively investigated [11], only the welds that used a rotation speed of 457 rpm and a welding speed of 457 mm/min were instrumented. When making the welds the tool was raked 1° away from the direction of travel. The plates were cleaned with a wire brush prior to welding which was necessary to produce satisfactory welds.

Table 1. Comparison between the dimensions of the Triflute™ and Trivex™ tools.

Distance from shoulder (mm)	Moment of inertia (mm^4)		Tool area/ Swept area	
	Triflute™	Trivex™	Triflute™	Trivex™
0	365	336	83%	78%
1	276	287.6	76%	78%
5.8	106	127	68%	75%

Table 2. Welding parameters used for the trials with the Trivex™ and Triflute™ tools.

Tool rotation speed (rpm)	Welding speed (mm/min) (Tools tested)			
457	367 (MX-Trivex™)	457 (Trivex™, MX-Trivex™ and MX-Triflute™)		
394	315 (MX-Trivex™)	394 (MX-Trivex™, and MX-Triflute™)	472 (MX-Trivex™, MX-Trivex™, and MX -Triflute™)	552 (MX-Trivex™, and MX -Triflute™)
	0.8	**1**	**1.2**	**1.4**
	Tool forward movement per revolution (mm)			

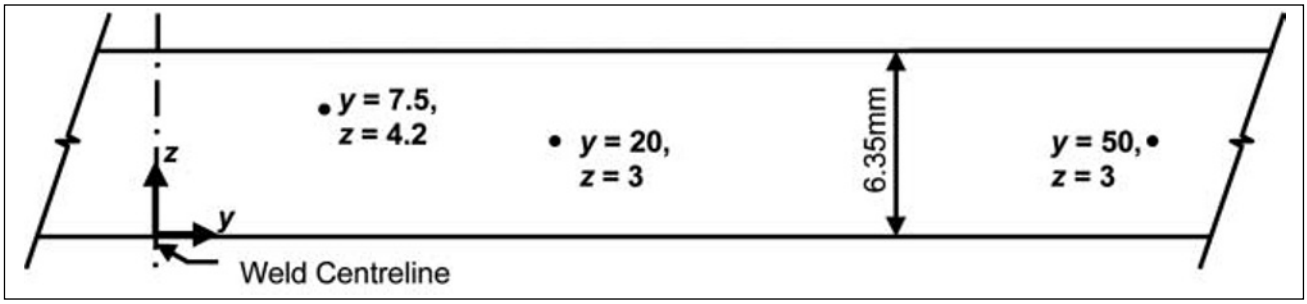

Fig. 7. Transverse section showing the locations of the thermocouples.

4.2 Forces

Figure 8a demonstrates how the traversing force was reduced by 18-25% with the new tool designs (the greater % reduction occurring at the lower speeds). The Trivex™ tool had a marginally lower traversing force than the MX-Trivex™ tool. This may be a consequence of the threads increasing the area carrying the limiting shear stress, which increases the traversing force for this shape. The traversing force increased with welding speed and the rotation speed had little effect for either tool. The increase in force with welding speed is a consequence of the greater volume of material needing to pass the tool per revolution. The following estimates of the traversing force were found for each tool:

$F = 0.013v + 5.54$ (5 – MX-Triflute™)

$F = 0.014v + 5.54$ (6 – MX-Trivex™)

where:

F = Traversing force (kN)

v = Welding speed (mm/min)

Figure 8b shows that the down force was similarly reduced by around 12% with the new tool concepts. The welding and rotation speeds had little effect on the value.

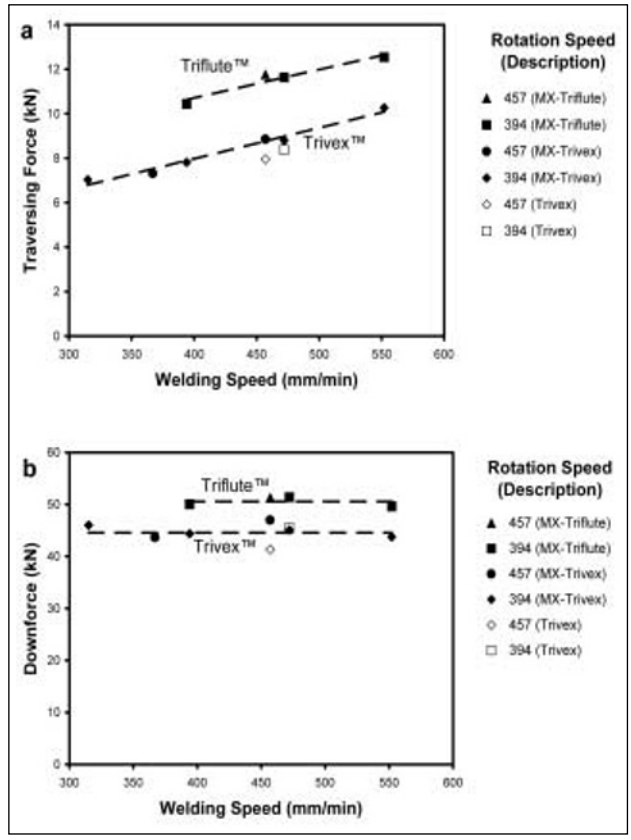

Fig. 8. Experimental (a) traversing and (b) down force results vs. welding speed.

4.3 Heat input and temperature

Figure 9 shows the weld power divided by the welding speed (i.e. heat input per mm of weld) for all the welds conducted. Additional results for the MX-Triflute™ tools are included from Colegrove and Shercliff [11]. There was little difference in the heat input for the different tool types with the Trivex™ tool using slightly more energy per mm than the Triflute™. Removing the threads on the Trivex™ tool had negligible effect on the power requirement.

The temperature results are shown in Figure 10 which demonstrates that there was little difference between

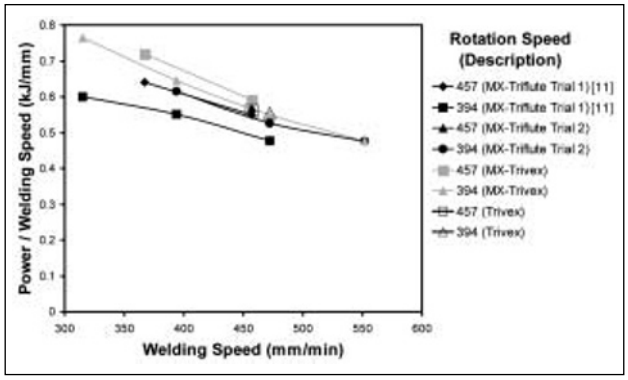

Fig. 9. Power divided by the welding speed (i.e. heat input per mm of weld) vs. welding speed.

the peak welding temperatures for the different tool types, with the exception of the MX-Triflute™ weld from the second trial which had a significantly higher weld temperature at all thermocouple locations.

The following factors were thought to cause the differences between the power inputs and weld temperatures:

a) Different backing bars. The first welding trial used a standard "screw type" backing plate made entirely of steel while the second trial used the new "vacuum" backing bar where the plates were clamped by a vacuum seal on either side of the weld. The vacuum backing plate used steel directly under the weld and a "slotted" aluminium plate (with high thermal conductivity) where the plates were clamped. This aluminium plate may have increased the heat loss, increasing the power required to make the weld.

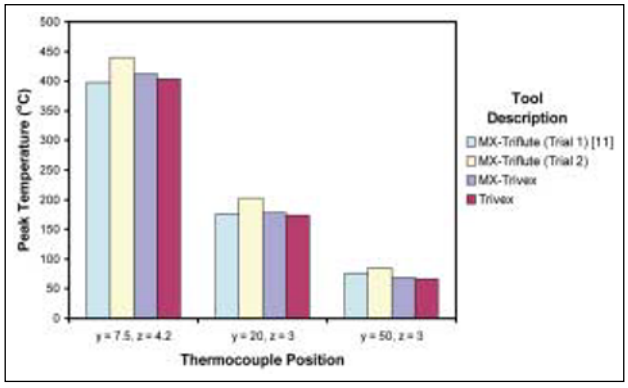

All welds used a rotation speed of 457 rpm and a welding speed of 457 mm/min.
Note that the Trivex™ and MX-Trivex™ results are an average of two readings.

Fig. 10. Peak temperature comparison at the three thermocouple locations.

b) Incomplete vacuum seal. On the latter welds that used the MX-Triflute™ tool, the vacuum seal progressively deteriorated enabling the plates to lift. This was thought to be the cause of the higher welding temperature for the second MX-Triflute™ weld.

c) Initial material temperature. A higher initial temperature reduces the power required to raise the material to welding temperature. The initial temperature for the welds in the first MX-Triflute™ trial was approximately 27 °C compared with 17 °C during the second trial.

d) Plunge depth. Colegrove and Shercliff [11] demonstrated that a high plunge depth increased the weld power and temperature, so variations in the plunge depth may have also contributed to the different readings.

To conclude, the different tool designs had little effect on the power requirement or the weld temperature. This result enables the same thermal model to be used for both the Triflute™ and Trivex™ tool designs in the following section.

4.4 Weld strength, material mixing

Tensile specimens were taken from several welds transverse to the welding direction. All the welds failed in the heat-affected zone except for one that used the MX-Triflute™ tool at the highest welding speed, which failed in the nugget. The welds made with the new tools matched the strength of the MX-Triflute™ at a welding speed of 473 mm/min with all welds having an ultimate tensile strength of 484 ± 6 MPa. A further comparison of the tensile strengths at a welding speed of 552 mm/min showed that the MX-Trivex™ tool had an average tensile strength of 488 MPa, which was marginally higher than the MX-Triflute™ tool with 470 MPa.

To aid visualisation of the material mixing along the joint line, a thin copper strip was placed in a small section of the joint line prior to welding. The final position after welding was determined by X-ray and indicated the degree to which the oxide at the interface was disrupted. This technique is described in Dickerson *et al*. [12]. Figure 11 shows that all three tools mixed the material well near the base. However, near the top the copper flowed around the tool with very little disturbance. This is because the shoulder, which does not disrupt the flow,

MX-Triflute™ MX-Trivex™ Trivex™

Note that the advancing side is on the right and the retreating side is on the left.

Fig. 11. Transverse X-ray cross-sections of copper placed in the welds.

has a much greater influence in this region. Surprisingly, even the Trivex™ tool without threads mixed the material well. There was much less copper visible in the X-ray of the MX-Trivex™ weld. This may be a consequence of poor copper placement and/or copper slippage through the plates while it was being welded.

4.5 Metallographic examination

Transverse sections of several of the welds were done to check weld integrity and are shown in Figure 12. The most noticeable difference between the three welds is in the shape of their weld nugget, particularly on the advancing side. While the nugget boundary with the MX-Triflute™ tool is perpendicular to the plate, the tools that used the Trivex™ tools widened toward the shoulder. This suggests that the Trivex™ shape encourages greater material movement near the top of the weld.

All welds were free of defects, however there is a small line of oxide around the centre of the Trivex™ weld where the material was less heavily deformed. This is enlarged in Figure 13a and also demonstrates a distinct surface layer. The surface layer was observed in the MX-Trivex™ and MX-Triflute™ welds, but was less severe.

Finally the thermomechanically affected zone (TMAZ) at the bottom of the weld on the advancing side is shown for the Trivex™ and MX-Trivex™ tools in Figures 13b and 13 c. There is a significant upsurge in the material with the Trivex™ tool which is typical of most welds. Interestingly, the upsurge while still present with the MX-Trivex™ tool was significantly reduced and the grains in the TMAZ were not deformed 90° to the plate surface near the weld nugget. The reason for this different flow characteristic is unclear and is not predicted by the 3 dimensional flow models described in a later section. At a higher welding speed the upsurge was reduced even further. This flow characteristic may have some interesting ramifications for lap welds where interface hooking in the TMAZ on the advancing side is one of the main concerns.

5 THERMAL MODEL

5.1 Introduction

Accurate 3 dimensional flow models of FSW require a prediction of the 3 dimensional thermal profile around the tool. Rather than coupling this calculation to the already complex flow model, a separate thermal model was created for this purpose and the results interpolated onto the flow model. The thermal model was a modified version of the one described in Colegrove and Shercliff [11] so only the key features and the differences with the previous work are described.

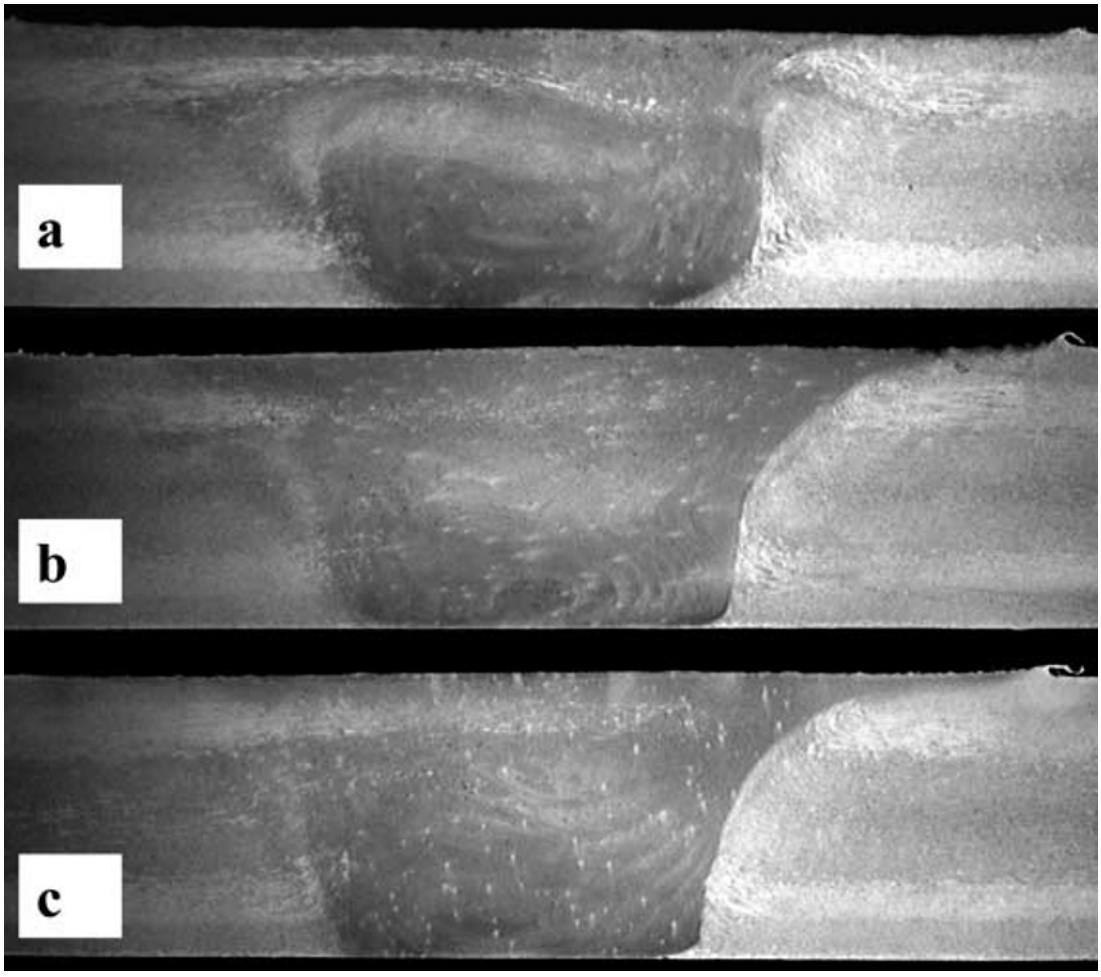

Fig. 12. Transverse sections of welds done with a rotation speed of 394 rpm and a welding speed of 473 mm/min for the
(a) MX-Triflute™ tool; (b) Trivex™ tool; (c) MX-Trivex™ tools.

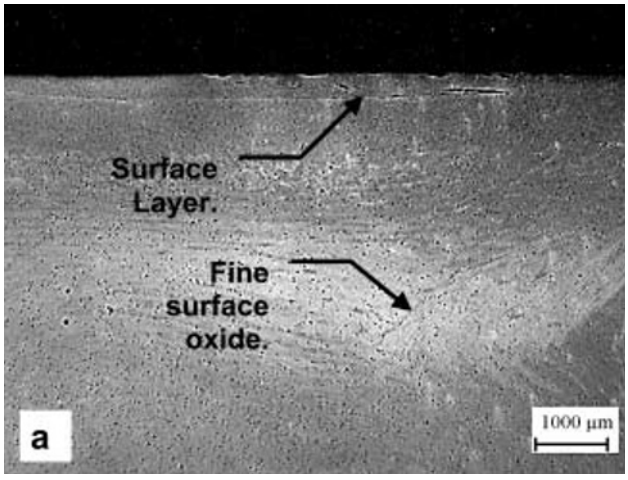

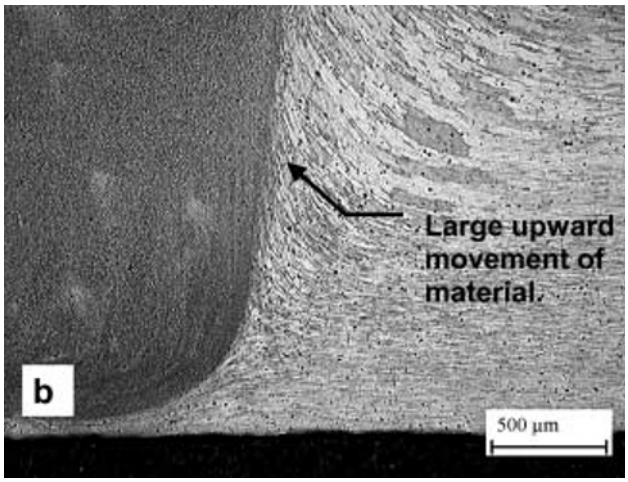

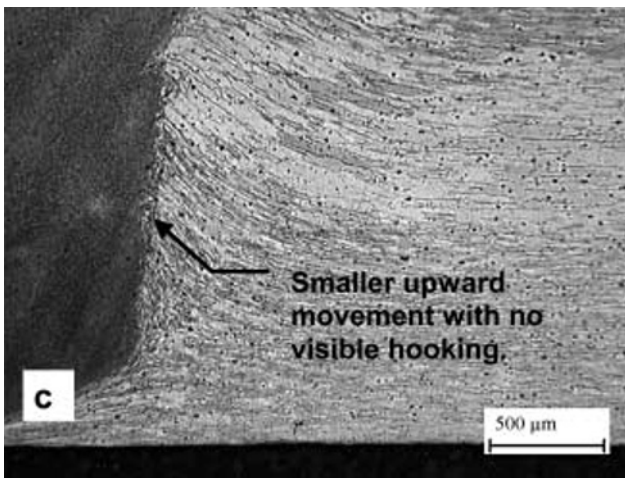

All welds used a rotation speed of 394 rpm and a welding speed of 473 mm/min.

Fig. 13. (a) Oxide layer in the nugget of the Trivex™ weld; TMAZ on the bottom advancing side for the (b) Trivex™ and (c) MX-Trivex™ welds.

As discussed earlier, the difference in heat input between the various tool types was small, so the same thermal model was used for all the tools. The weld power and temperature results from the welding trial reported in Colegrove and Shercliff [11], which used a MX-Triflute™ tool, were used to validate the model.

The welding conditions used for the thermal models are described in Table 3. Although no temperature results were available for the 552 mm/min weld, the thermal profile was found from a model that used the same set-up as the validated models with the experimentally measured heat input.

Table 3. Welding parameters used for the thermal and flow models.

Tool rotation speed (rpm)	Welding speed (mm/min)			
457	367	457		
394	315	394	472	552
	0.8	**1**	**1.2**	**1.4**
	Tool forward movement per revolution (mm)			

5.2 Model description

FLUENT was used for the thermal model because it enabled the inclusion of the approximate convective heat flow round the tool through a crude prediction of the material flow, and also the ready interpolation of results onto the flow model. In FSW the tool generates heat via a combination of friction at the tool surface and viscous dissipation within the deformed material. This heat is conducted into the tool and welded material, and is then convected from the top surface or conducted into the backing plate. In the model, a uniform heat flux was applied on the annular surface of the shoulder and the conical surface of the pin. The heat flux at the pin (power/unit area) was twice that at the shoulder, which enabled better correlation between experimental and numerical thermal profiles. Unlike the model reported in Colegrove and Shercliff [11], the actual heat input from the weld was used to calculate the heat flux. These values were between 21 and 36% greater than the numerical values previously used. This greater heat input was offset by a greater heat loss to the backing plate, which is discussed below.

Figure 14 shows the mesh used for the thermal models, which used a featureless pin. The tool and backing plate were included to calculate the heat loss to these regions.

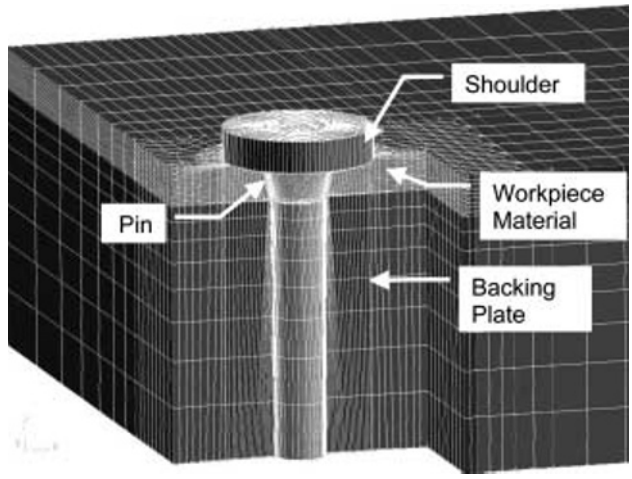

Fig. 14. Section through the mesh used for the thermal models.

In an effort to keep the model small, a single layer of elements was used for the tool. However unlike the model in Colegrove and Shercliff [11] a complete backing plate of thickness 40 mm was included. A conduction zone where heat loss was calculated by the one-dimensional heat equation was defined on the top surface of the tool. The tool thickness was arbitrarily set to 100 mm for this calculation.

To model the incomplete contact between the welded material and the backing plate a contact resistance was used. This is the most uncertain aspect of the model since there is a lack of published data, and its value is highly dependent on the pressure between the contacting surfaces. The model used perfect contact under the shoulder and a value of 1 000 mm^2K/W in the far field. This enabled good agreement between experimental and numerical thermal profiles. The difference was caused by the much higher interface pressure under the shoulder which aided heat flow. In the previous model a value of 100 mm^2K/W was used underneath the shoulder and 1 250 mm^2K/W in the far field. The current model has greater heat loss to the backing plate to offset the greater heat input.

The convective heat flow around the tool was included through a crude prediction of the material flow. This feature smoothes the temperature profile near the tool enabling a more accurate prediction of the weld temperature. The prediction was obtained by calculating the flow for a “stick” model using the 7075 material properties as in the 2 dimensional models [6]. Finally, the convective heat loss from the top surface of the aluminium plate was calculated with a convective heat transfer coefficient of 10 W/m^2K.

The thermal material properties were the same as those used in Colegrove and Shercliff [11]. Temperature dependent values from Mills [21] were used for the aluminium, while temperature independent values for steel from Holman [22] were used for the tool and backing plate.

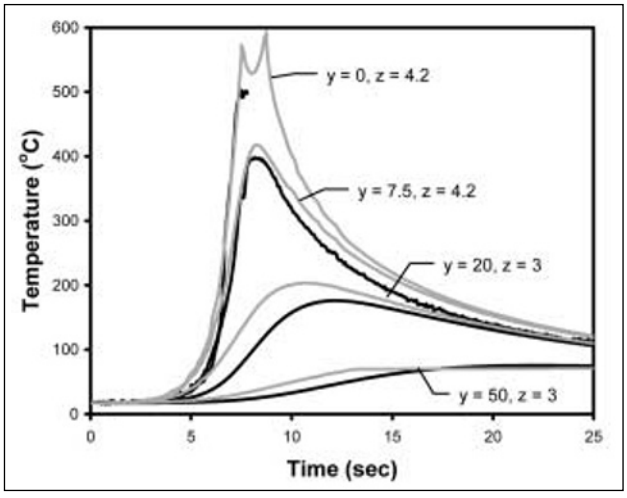

Fig. 15. Comparison between numerical (grey) and experimental (black) temperature profiles for the weld that used a rotation speed of 457 rpm and a welding speed of 457 mm/min.

5.3 Thermal results

Figure 15 shows a comparison between the experimental and numerical temperature profiles for the weld that used a rotation speed of 457 rpm and a welding speed of 457 mm/min. Note that the correlation for this weld was one of the poorest. Figure 16 shows the corresponding contour plot, which clearly shows how the thermal contact resistance reduced the conduction of heat into the backing plate.

6 THREE DIMENSIONAL FLOW MODELS

This section describes the development of 3 dimensional models of the Trivex™ and Triflute™ tools. These models use a modified version of the slip boundary condition developed for 2 dimensions [6].

6.1 Mesh

Figure 17 shows one-third sections of the meshes that were used for the flow models. Only the region near the tool was included to keep the model small. To simplify the geometry the tool threads, the tool rake angle, the

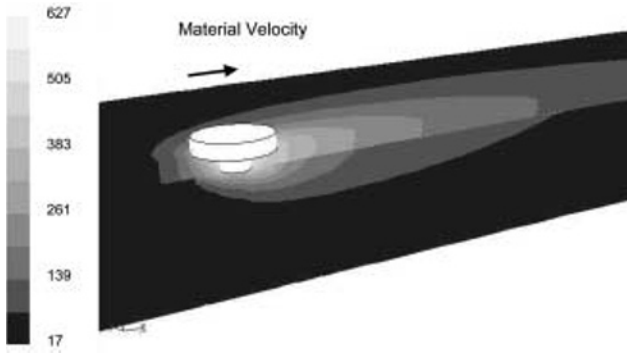

Fig. 16. Predicted thermal contours (°C) for the weld that used a rotation speed of 457 rpm and a welding speed of 457 mm/min.

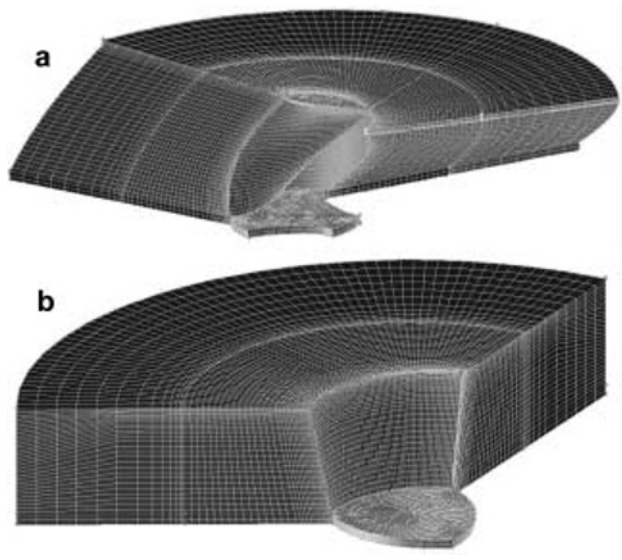

Fig. 17. Mesh for (a) Triflute™ and (b) Trivex™ tools.

concentric ring on the shoulder and the radiused tip of the tool were omitted (see Figure 6). It is anticipated that all these features have a second order effect on the results. The effect of a tool thread on the Trivex™ tool was investigated earlier and showed that while the nugget shapes were similar, the flow in the TMAZ was significantly different.

Although the stick models could be solved with tetrahedral elements these caused large velocity discontinuities when applied with the slip boundary condition. Therefore hexahedral elements were used for both models. Tests were done to ensure that the mesh density and number of iterations were sufficient. Finally, note that the mesh used for the Triflute™ tool in Figure 17a used a thin layer of undistorted hexahedral elements adjacent to the shoulder. This avoided the use of distorted elements in a region where the velocity gradient was high.

6.2 Model setup

The model developed in FLUENT used the following boundary conditions: The top surface outside the shoulder, the side walls and the bottom surface were all given a velocity equal to the welding speed. The shoulder and pin were given a velocity equal to the rotation speed for the stick model or the shear stress was specified for the slip model. The code used for the slip boundary condition is described in Appendix A and was a modified version of that used for the 2 dimensional models described in Colegrove and Shercliff [6]. A single rotating reference frame is used for the material around the tool. All the models analysed are steady-state where the solution is a “snap-shot” of the flow at a particular instant in time.

7075-T6 aluminium alloy was selected for the modelling work. The material property of most interest is the viscosity, which was interpolated from experimental stress vs. strain-rate data produced by Jin *et al.* [8] and implemented in FLUENT through user-defined code. The values were interpolated on a logarithmic scale with strain rate and a linear scale with temperature.

7 RESULTS AND DISCUSSION

7.1 Isothermal models

Isothermal models were solved to gain a good understanding of the model characteristics while retaining a simple problem. The isothermal models assumed a material temperature of 527 °C. Since the flow stress of 7075 at high temperature is not greatly affected by the temperature [8] and the temperature variation across the intense deformation zone is relatively small, the assumption is reasonable for a first analysis.

All the models used a welding speed of 457 mm/min and a rotation speed of 457 rpm. Five different boundary conditions were used on the shoulder and pin. The first was the stick condition and the rest were slip conditions where the limiting shear stressed ranged from 80 to 10 MPa. For the slip models an identical limiting shear stress was used on the shoulder and the pin.

Figure 18 shows the traversing and down forces for the different models (down force is given for the pin only). Note that the down force for all the Trivex™ models was near zero so this was not included in the plot. The traversing forces for the Triflute™ and Trivex™ tools were very similar for the stick, and 80 MPa and 40 MPa slip models. It was only the slip models that used limiting shear stresses of 20 and 10 MPa where the Trivex™ shape showed a significant advantage over the Triflute™. Note that the 2 dimensional models showed significant advantages when the limiting shear stress was 40 MPa. The difference may be a consequence of the shoulder’s effect on the material flow. The down force with the Triflute™ tool gradually increased with reduced limiting shear stress. The greater the slip, the greater the material “screwing” effect and therefore the greater the down force measured by the model.

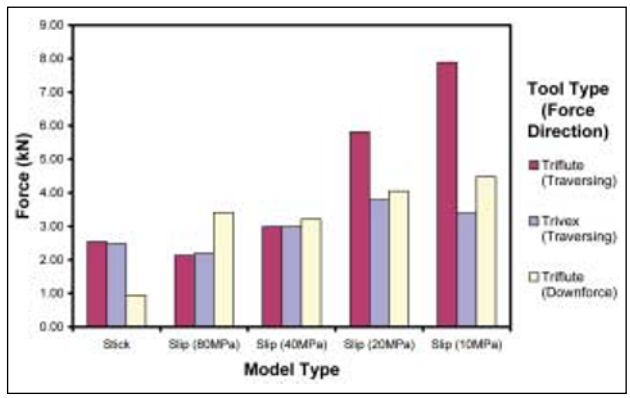

Fig. 18. Comparison between the traversing and down forces for the different isothermal models.

Figure 19 shows streamline plots for the models that used a limiting shear stress of 40 MPa. Note that streamlines are instantaneously parallel to the flow and are shown for a particular tool orientation. Particle tracks are much more difficult to calculate and require a full transient analysis. Unfortunately, the complexity of the flow meant that several of the tracks were lost in the case of the Trivex™ tool or never escaped with the Triflute™ tool. Nevertheless, the streamlines demonstrate several important process characteristics. Firstly both tool profiles demonstrate that all the material that is in line with the tool is swept round the retreating side. The main difference between the two tools is in the vertical movement of material. The Triflute™ tool augers the material in the flutes downwards, which causes the material in the far field to be pushed upwards. This effect is seen clearly in Figure 19b, which shows the upward movement of a streamline that initially started on the centreline. Figure 20 shows a macrosection from a 16 mm weld that used a MX-Triflute™ tool. This clearly demonstrates the upward flow in the TMAZ confirming the prediction of the model. The upward movement of material that was also observed with the Trivex™ tool cannot be explained by the current model.

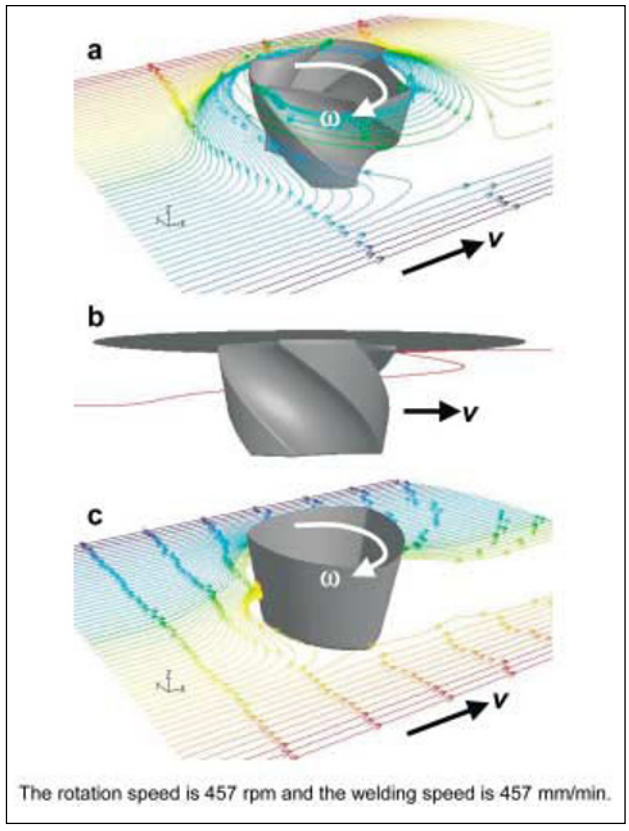

Fig. 19. Steamlines for the isothermal models that used a limiting shear stress of 40 MPa:
(a) Triflute™ tool
(b) single streamline for Triflute™ tool showing vertical movement and
(c) Trivex™ tool

7.2 Torque calibrated isothermal models

The next step in developing a model that represents the "real" welding conditions is to calibrate the limiting shear stress so that the model torque (and by inference power) matched the experimental value. Appendix B describes how this was implemented in FLUENT. Results indicated that the limiting shear stress ranged between 14 to 22 MPa. Figure 21a shows a comparison between the numerical and experimental traversing forces. The model under-predicts the traversing force by about 60% with the Trivex™ tool and 35% with the Triflute™ tool. One cause of this under-prediction was the use of isothermal material properties. Interestingly, the rotation speed had very little effect on either the experimental or numerical results.

The elastic properties of the material were neglected in the model. While this assumption has little effect on the rotational flow, it does impact on the model's ability to predict the vertical down force. Therefore, a better comparison was to subtract the down force of the Trivex™ pin from the Triflute™ pin for both the model and the experiments, which is shown in Figure 21b. Both the model and experiment indicate higher down forces with the Triflute™ than with the Trivex™, reflecting the augering action of the flutes. The numerical predictions were within 37% of the experimental values and both were largely independent of the welding speed. It is difficult to comment on the effect of rotation speed because only one experimental value was obtained at the higher speed.

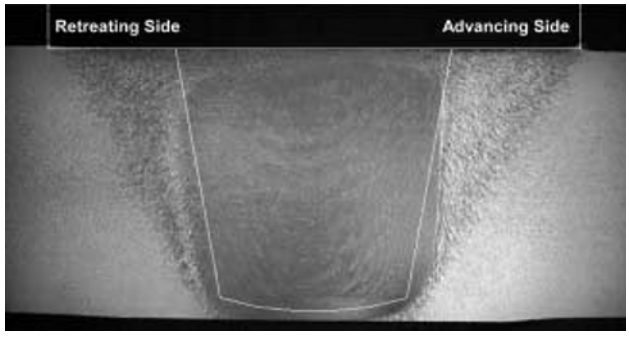

Fig. 20. Macrosection from a 16 mm weld with an MX-Triflute™ tool with an overlay of the tool profile.

7.3 Torque calibrated models with an interpolated temperature profile

A flow chart describing the operation of these models is shown in Figure 22. The effect of temperature on the material properties is included by interpolating the temperature profile from the thermal model described previously. Like the models in the previous section, the limiting shear stress was adjusted so that the torque matched that from the experiment. This completed the loop so that the model gave the best possible estimate

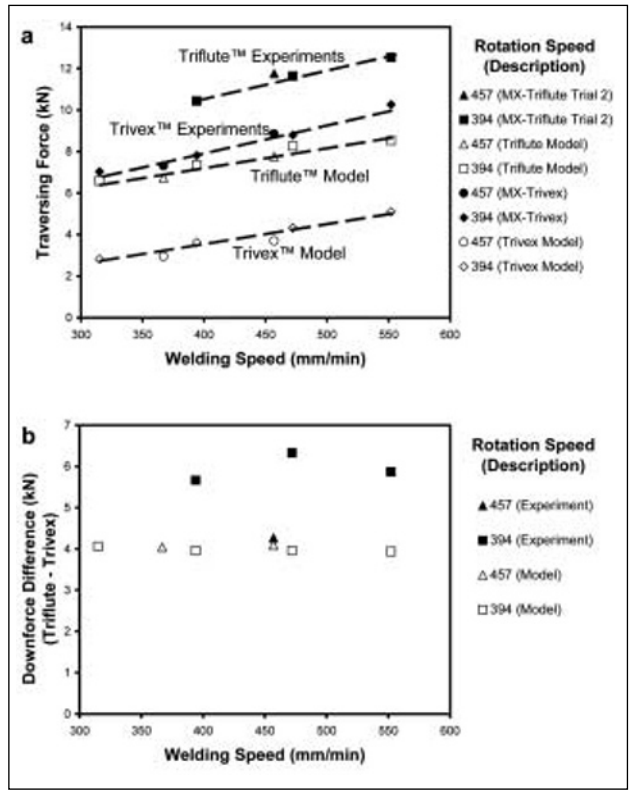

Fig. 21. Comparison between measured and predicted forces.
(a) traversing force
(b) down force difference (Triflute™ - Trivex™) for the torque calibrated isothermal models.

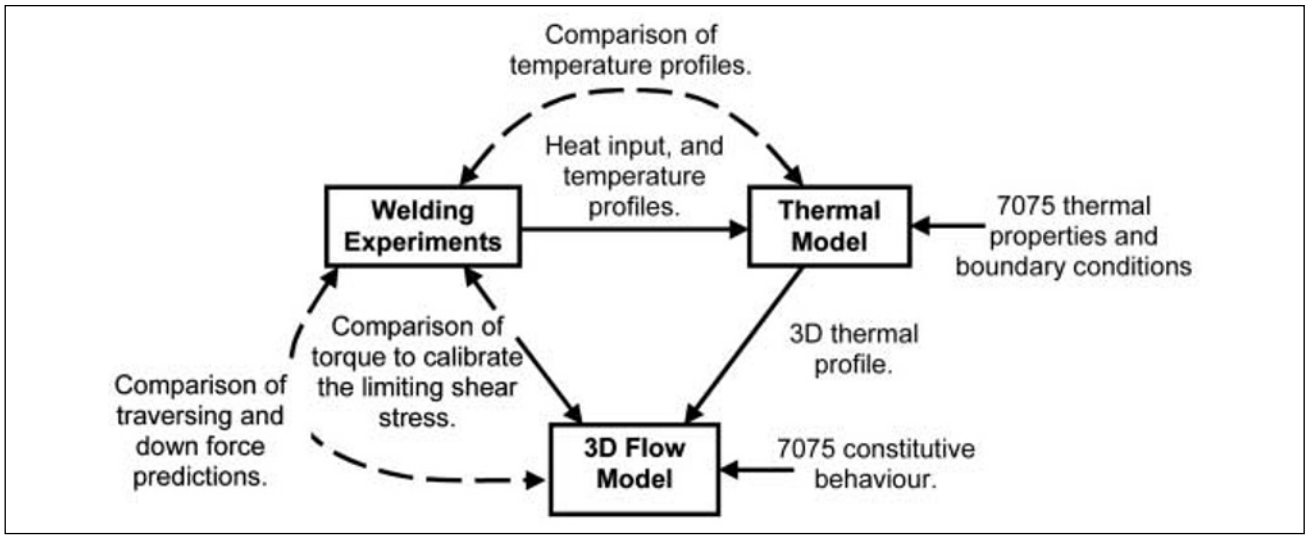

Fig. 22. Flowchart describing the torque calibrated temperature profile models.

of the "real" welding conditions. It should be noted that the interpolated temperature profile was not uniform and had spikes that affected the accuracy of the results. This problem is discussed in more depth in Colegrove [23].

Figure 23a shows the limiting shear stress required for each of the models. The temperature profile models generally required a slightly smaller limiting shear stress than their isothermal counterparts in the previous section. Quite possibly the harder, lower temperature material (especially around the base of the pin) required a lower limiting shear stress to generate the same torque (and heat).

As expected the values increased with welding speed because of the greater heat input required for these models. The Trivex™ tool required a marginally greater value than the Triflute™ tool. This is because this shape does not "stir" the material quite as efficiently as the Triflute™. Comparing the values for the different rotation speeds, the limiting shear stress for the 457 rpm welds was marginally higher than the welds that used a rotation speed of 394 rpm. This is caused by two opposing effects. Firstly, from the welding experiments reported in Colegrove and Shercliff [11] the welds that used a higher rotation speed required more weld power. However the higher rotation speed lowers the required torque, T because:

$$T = \frac{P}{\omega} \tag{7}$$

where P is the weld power and ω is the rotation speed, i.e. both P and ω are increased at the higher rotation speed. Therefore there is only a small difference in the required torque and hence the limiting shear stress at the higher rotating speed.

The heat input at the pin and shoulder were found by multiplying the respective torques by the rotation speed. Figure 23b shows how the ratio of pin heat to total heat compared for the two models. As stated above the same limiting shear stress was used on both the shoulder and pin. This was considered the best first estimate in the absence of a more detailed understanding. With this assumption it was found that the pin heat to total heat ratio reduced with increasing welding speed. This is because the heat produced at the shoulder is directly proportional to the limiting shear stress, while that produced by the pin is also influenced by the pin profile, i.e. even with a zero limiting shear stress the pin profile will stir the material. This may be represented by the following (approximate) relationships

$$P_s \approx C_1 \tau_{\max} \tag{8}$$

$$P_p \approx C_2 \tau_{\max} + K \tag{9}$$

where:

P_s is the shoulder power.

P_p is the pin power.

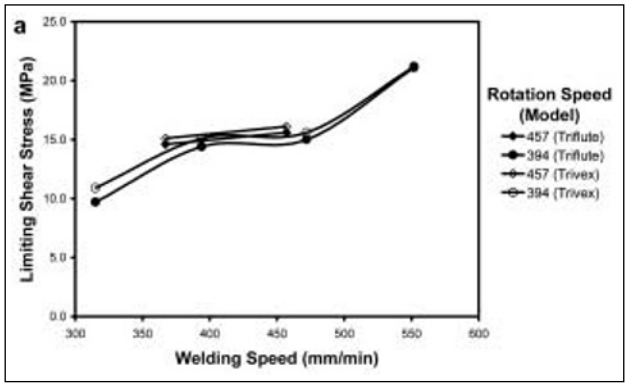

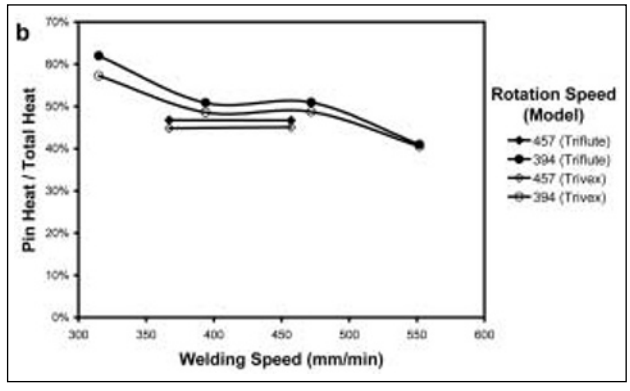

Fig. 23. Comparison between:
(a) limiting shear stress and (b) pin heat to total heat ratio for the Triflute™ and Trivex™ models.

C_i are constants.

K is the power when the limiting shear stress is zero.

τ_{max} is the limiting shear stress.

Therefore, with a low limiting shear stress the pin heat dominates, while at higher values the shoulder heat becomes more significant. Interestingly, in the thermal model described above the heat flux at the pin was assumed to be twice that at the shoulder because there was better agreement between the numerical and experimental thermal profiles. This assumption gives a ratio of pin heat to total heat of 51%, which is remarkably similar to that obtained with the uniform limiting shear stress assumption.

Figure 24a shows a comparison between the numerical and experimental traversing forces. The values were higher than those obtained from the isothermal model and were up to 100% higher than the experimental values for the Triflute™ tool, but up to 36% lower than the experimental values for the Trivex™ tool. One possible reason for the discrepancy is that more of the weld power needs to be apportioned to the pin and less to the shoulder. To generate the higher power input at the pin, a higher limiting shear stress is required (at the pin). This will increase the welding force with the Trivex™ shape and reduce it with the Triflute™ shape. Another reason for the discrepancy is the problem in the interpolated temperature profile mentioned earlier. Finally, the model indicates a reduction in the traversing force with increasing rotation speed (particularly for the Triflute™), which does not agree with the experimental findings.

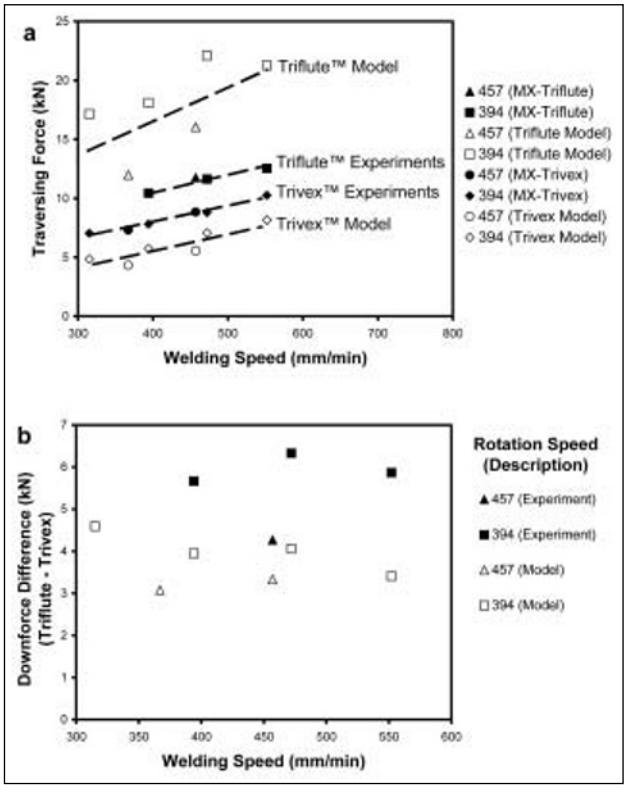

Fig. 24. Comparison between measured and predicted forces: (a) traversing force (b) down force difference (Triflute™ - Trivex™) for the torque calibrated temperature profile models.

The downforce difference comparison between the numerical and experimental values is shown in Figure 24b. The results are similar to those obtained with the isothermal model in the previous section, except that the rotation speed now has an influence on the value in line with the (limited) experimental evidence.

Figure 25 shows a comparison between the strain-rate = 2/s boundary for an isothermal model and one that included the temperature profile. Both used the torque to calibrate the limiting shear stress and a welding speed of 457 mm/min and a rotation speed of 457 rpm. Previous work [6] has shown that the strain-rate = 2/s boundary approximates the border between the deforming and undeforming material. This result clearly shows how the size of the deformation region is reduced with the introduction of the thermal profile.

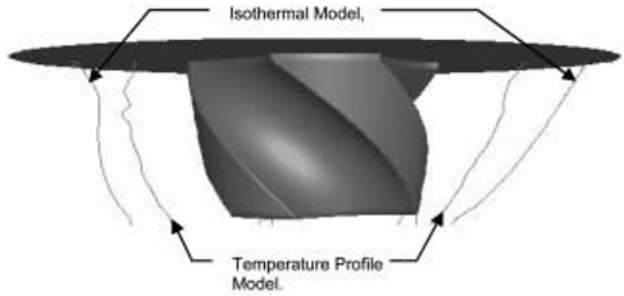

Both models are torque calibrated and used a Triflute™ tool with a welding speed of 457 mm/min and a rotation speed of 457 rpm.

Fig. 25. Comparison of the deformation region size (strain-rate = 2/s boundary) for an isothermal model and one that included the temperature profile.

Figure 26 shows the streamlines at mid-section for both profiles, with a welding speed of 473 mm/min and a rotation speed of 457 rpm. The complexity of the flow meant that the streamlines that passed near the tool surface could not be followed. Like the isothermal models the plots indicate that material in line with the pin is swept round the retreating side. However, the deformation region is much narrower which is indicated by the proximity of the first streamline on the advancing side of the tool, which passes without being stirred into the rotational flow. Like the isothermal models much greater vertical movement is observed with the Triflute™ tool due to its augering action.

8 CONCLUSIONS

This work has demonstrated the development and benefits of the Trivex™ tool over the conventional MX-Triflute™ tool. This tool was developed from 2 dimensional models that indicated that the traversing force could be minimised with this profile. Experiments verified this result and showed that the properties of the welded material equalled and in some cases exceeded that of the MX-Triflute™ tool.

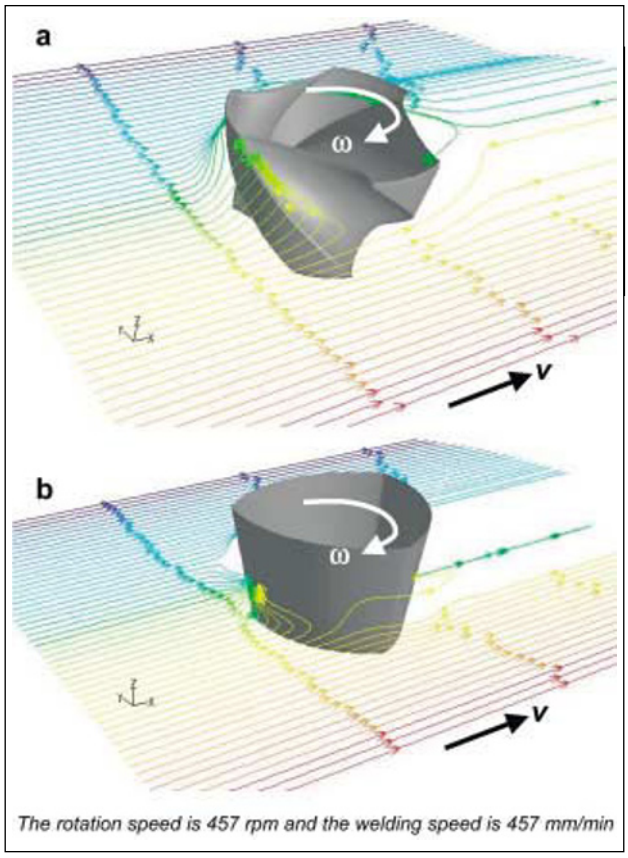

Fig. 26. Streamline plots for: (a) Triflute™ ; (b) Trivex™ tool shapes, that included the temperature profile.

There was very little difference in the heat input or weld strength for the different tool shapes, and experiments with copper marker material indicated that the new tools effectively mixed the material in the weld nugget. However metallographic examination revealed a thin layer of oxide in the centre of the Trivex™ weld nugget.

Three dimensional thermal models that used the experimental heat input predicted the weld thermal profile, which correlated well with the experimental curves. The output of the thermal model was used for the subsequent 3 dimensional flow models.

The 3 dimensional flow models confirmed the benefits of the Trivex™ profile over the Triflute™ profile. Two different model types were compared: an isothermal model, and one that included the thermal profile. Predictions of the weld traversing and down forces from these models compared favourably with the experimental results given the complexity of the problem. In particular, the predictions from the thermal profile model were slightly higher than those from the isothermal model, particularly for the Triflute™ tool. It may be argued that the predictions of the traversing force from the isothermal model are sufficient provided an appropriate "safety factor" is used.

Streamline plots were used to assist understanding of the material flow around the tool. These demonstrated the strong augering action of the Triflute™ tool, which caused this tool's higher down force.

The work also demonstrated several novel modelling techniques. The first was the slip boundary condition in 3 dimensions, where a limiting shear stress was applied at the surface and the material was allowed to slip against the tool. The second involved adjusting the limiting shear stress so that the weld power of the model matched that obtained experimentally. The final technique was the inclusion of the temperature profile by interpolating the result from a thermal model. This obviated the need to solve the thermal profile in conjunction with the flow model.

Future work with the Trivex™ and MX-Trivex™ tools, will focus on steel where the potentially lower traversing force will be advantageous and lap welds where the different flow characteristics may help minimise hooking of the interface on the advancing side. Finally, the numerical models may be used to predict the weld traversing force for sizing the FSW pin, which will be a significant advance over the current "trial and error" approach.

ACKNOWLEDGEMENTS

The authors wish to express their thanks to the University of Adelaide, The Welding Institute (TWI), the UK Department of Trade and Industry (DTI), the University of Cambridge, the Post-Graduate Training Partnership (PTP), and the Cambridge Commonwealth Trust for their financial support. The advice given by Chris Dawes and Philip Threadgill and the technical assistance of Adrian Addison and Terry Dickerson was greatly appreciated.

REFERENCES

1. Thomas W.M., Nicholas E.D., Needham J.C., Murch M.G., Temple-Smith P., Dawes C.J.: Friction stir butt welding, Int. Patent Application No. PCT/GB92/02203; GB Patent Application No. 9125978.8, 1991; US Patent No. 5460317, 1995.

2. Thomas W.M., Nicholas E.D., Needham J.C., Murch M.G., Temple-Smith P., and Dawes C.J.: Improvements relating to friction welding, International Patent Classifications B23K 20/12, B29C 65/06, 1993.

3. Shercliff H.R., Colegrove P.A.: in "Mathematical Modelling of Weld Phenomena 6", (ed. H. Cerjak, and H.K.H.D. Bhadeshia), 927-974; 2002, London, Maney Publishing.

4. Xu S., Deng X., Reynolds A.P., Seidel T.U.: Sci. Technol. Weld. Joining, 2001, 6(3), 191-193.

5. Seidel T.U., Reynolds A.P.: Sci. Technol. Weld. Joining, 2003, 8(3), 175-183.

6. Colegrove P.A., Shercliff H.R.: "2-Dimensional CFD modelling of flow round profiled FSW tooling", Sci. Technol. Weld. Joining, (in press).

7. FLUENT, Release 6.0.20, Fluent Incorporated, 2002, Lebanon, NH.

8. Jin Z., Cassada W.A., Cady C.M., Gray G.T.: in "Material Science Forum" Vols. 331-337, 527-532; 2000, Switzerland, Trans Tech Publications.

9. Thomas W.M., Gittos M.F.: Development of friction stir tools for the welding of thick (25 mm) aluminium alloys, TWI Core Research Report No. 692/1999, Cambridge, UK, 1999.

10. Dawes C.J.: Friction Stir Welding of Transport Structures - Phase II - Final Report, Report No. 12030/13/01, TWI Ltd, Cambridge, UK, 2001.

11. Colegrove P.A., Shercliff H.R.:"Experimental and numerical analysis of 7075-T7351 Friction Stir Welds", Sci. Technol. Weld. Joining, (in press).

12. Dickerson T., Schmidt H., Shercliff H.R.: in Proc. 4th Int. Symp. on "Friction Stir Welding", Park City, Utah, 2003, TWI Ltd.

13. Askari A., Silling S., London B., Mahoney M.: in "Friction Stir Welding and processing", (Ed. K.V. Jata *et al.*) 43-54; 2001, Warrendale, PA, TMS.

14. Bendzsak G.J., North T.H., Smith C.B.: Proc. 2nd Int. Symp. on "Friction Stir Welding", Gothenburg, Sweden, 2000, TWI Ltd.

15. Colegrove P.A., Painter M., Graham D., Miller T.: Proc. 2nd Int. Symp. on "Friction Stir Welding", Gothenburg, Sweden, 2000, TWI Ltd.

16. Colegrove P.A., Shercliff H.R.: 3 Dimensional CFD modelling of flow round a threaded tool profile, submitted to Journal of Materials Processing Technology.

17. Goetz R.L., Jata K.V.: in "Friction Stir Welding and Processing", (Ed. K.V. Jata *et al.*) 35-42; 2001, Warrendale PA, TMS.

18. Dong PLu., F., Hong J.K., Cao Z.: Sci. Technol. Weld. Joining, 2001, 6(5), 281-287.

19. Ulysse P.: International Journal of Machine Tools and Manufacture, 2002, 42, 1549-1557.

20. Xu S., Deng X.: Proc. 4th Int. Symp. on "Friction Stir Welding", Park City, Utah, May 2003, TWI Ltd.

21. Mills K.C.: Recommended values of thermophysical properties for commercial alloys, 68-71; 2002, Cambridge, UK, Woodhead Publishing Ltd.

22. Holman J.P.: Heat transfer, seventh edition in SI Units, 651-653; 1990, London, McGraw-Hill Book Company.

23. Colegrove P.A.: Modelling of Friction Stir Welding, PhD Thesis, The University of Cambridge, Cambridge, UK, 2003.

APPENDIX A: APPLYING THE SLIP BOUNDARY CONDITION IN 3 DIMENSIONS

A.1 Defining the shear stress and relative velocity in 3 dimensions

Define two vectors:

$$\mathbf{n} = (x_n, y_n, z_n) \quad \text{(A.1)}$$

$$\frac{\omega}{|\omega|} = (0,0,-1) \quad \text{(A.2)}$$

The first is the normal unit vector at point P, which points toward the tool surface. The second is the unit direction vector for rotation, which is negative for clockwise rotation. Point P, and the surface normal are shown in Figure A.1a.

$\mathbf{d}_{tan}$, which is also shown in Figure A.1a is a unit vector which is parallel to the tool surface and perpendicular to the direction of rotation and is defined by:

$$\mathbf{d}_{tan} = \mathbf{n} \times \frac{\omega}{|\omega|}$$

if $d_{tan} < 0.001$ then

$$\mathbf{d}_{tan} = -\mathbf{P} \times \frac{\omega}{|\omega|} \quad \text{(A.3)}$$

where P is the position vector.

$$\mathbf{d}_{tan} = \frac{\mathbf{d}_{tan}}{|\mathbf{d}_{tan}|} \quad \text{(A.3)}$$

$\mathbf{d}_{tan}$ is defined differently to the definition used for 2 dimensions in Colegrove and Shercliff [6]. Firstly the value is normalised to ensure that it has a magnitude of 1. Secondly an "if" statement is used to check whether $\mathbf{d}_{tan}$ is small. This occurs where the surface normal is in the same direction as the rotation axis. i.e. at the shoulder. In this case the direction of the applied stress will

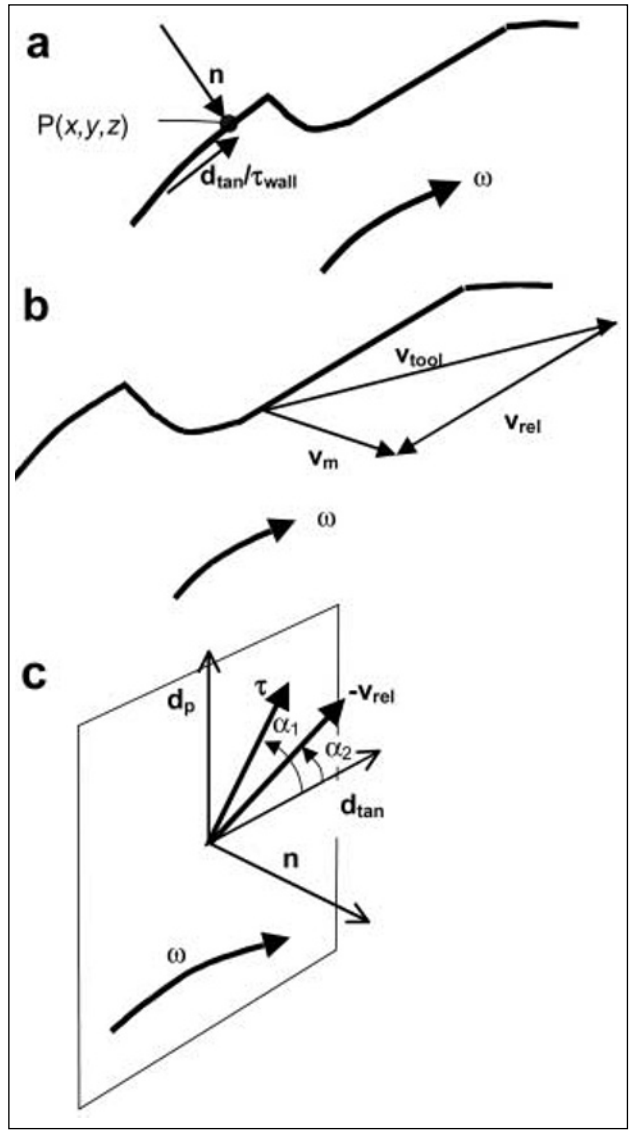

Fig. A.1 Description of: (a) the normal vector and d_{tan}; (b) the velocity vectors at the tool surface; and (c) the vectors d_p and τ and $v_{rel.}$

be in the direction of rotation, which is found from the cross product of the position vector and the rotation vector.

The relative velocity magnitude is found in an identical way to the 2 dimensional code except that the third dimension is included. i.e.

$$\mathbf{v}_{rel} = \mathbf{v}_m - \mathbf{v}_{tool} \quad (A.4)$$

where:

$\mathbf{v}_{tool}$ = Tool velocity

$= -\mathbf{r} \times \omega$

$\mathbf{v}_m$ = Material velocity

$\mathbf{v}_{rel}$ = Velocity of the material relative to that of the tool. Note that this velocity must always be parallel to the surface of the tool.

These vectors are shown diagrammatically in Figure A.1b.

A.2 Applying the shear stress

Applying the shear stress in 3 dimensions is more complex than 2 because the material can also slip in the direction of the rotation axis ω. This was particularly pertinent to the Triflute™ tool, which "screws" the material downwards. Therefore the applied shear stress opposes the flow of the slipping material. i.e. its direction is opposite to the relative velocity $\mathbf{v}_{rel}$ rather than being in the direction of $\mathbf{d}_{tan}$ which was the case in 2 dimensions.

It is impossible to arrive at the final solution in a single step so a conventional stick model is solved before being converted to the slip model. On the first iteration of the slip model, $\mathbf{v}_{rel}$ equals zero so there is no velocity component parallel to the rotation axis ω. Therefore the wall shear stress is given by:

$$\tau_{wall} = \tau_{max} (\mathbf{d}_{tan}) \quad (A.5)$$

On subsequent iterations where there is flow in the 3rd dimension, (i.e. down the tool flutes) the shear stress is given by:

$$\tau_{wall} = \tau_{max} \frac{\mathbf{v}_{rel}}{|\mathbf{v}_{rel}|} \quad (A.6)$$

Unfortunately implementing equation (A.6) led to an unstable solution because the direction of the surface velocity and hence the applied wall shear stress was unstable. To rectify this problem the following additional code was implemented:

Define the vector $\mathbf{d}_p$ which is perpendicular to both $\mathbf{n}$ and $\mathbf{d}_{tan}$. i.e.

$$\mathbf{d}_p = \mathbf{n} \times \mathbf{d}_{tan} \quad (A.7)$$

This is shown diagrammatically in Fig. A.1c. The angle that the current shear stress makes with $\mathbf{d}_{tan}$ can be found by:

$$\alpha_1 = \tan^{-1} \left(\frac{\mathbf{d}_p \cdot \tau_{wall}}{\mathbf{d}_{tan} \cdot \tau_{wall}} \right) \quad (A.8)$$

Similarly, find the angle that the negative of the relative velocity makes with the wall by:

$$\alpha_2 = \tan^{-1} \left(\frac{\mathbf{d}_p - \mathbf{v}_{rel}}{\mathbf{d}_{tan} \cdot - \mathbf{v}_{rel}} \right) \quad (A.9)$$

Finally, the new angle for the applied wall shear stress, α_3 is found by:

$$\alpha_3 = \alpha_1 + C (\alpha_2 - \alpha_1) \quad (A.10)$$

where C is a constant that determines the change from the old value. It was found that a relatively small value of 0.01 was necessary for a stable solution. Even though the value is small, the approximate error after 2000 iterations (which is typical) is:

$0.99^{1000} = 1.9 \times 10^{-9}$

Finally, the applied shear stress is found from:

$$\tau_{wall} = \tau_{max} (\cos \alpha_3 \mathbf{d}_{tan} + \sin \alpha_3 \mathbf{d}_p) \quad (A.11)$$

A.3 The slip boundary condition logic in 3 dimensions

A shear stress boundary condition is not only used where the material is slipping but where it is stuck to the tool. This is done because FLUENT does not allow the user to have a boundary where two different boundary conditions are set. i.e. stick where the material velocity is prescribed and slip where the shear stress is prescribed. Therefore where the material is stuck to the tool, the shear stress must be set so as to give zero relative velocity between the tool and material.

This section uses the following variables in addition to those defined in section 1:

- Shear_Max. Boolean variable, which has a value of 1 if the maximum shear stress is defined on the surface and slip occurs, and 0 if a no-slip boundary condition is defined.
- v_{relt}. Variable that defines whether the relative velocity is in the same or opposite direction to the tool velocity. It is found by:

$$v_{relt} = \mathbf{v}_{rel} \cdot \mathbf{v}_{tool} \quad (A.12)$$

If the material velocity is greater than the tool velocity then $\mathbf{v}_{rel}$ is in the same direction as the tool and $v_{relt} > 0$. Similarly, if it is less than or equal to the tool velocity then $v_{relt} \leq 0$.

The following steps were used when implementing the slip boundary condition:

- Step 1. Solve the system using a stick boundary condition and determine the shear stress at the wall.
- Step 2. If:

$|\tau| > \tau_{max}$

then the shear stress at the wall is given by equation (A.5) and Shear_Max is given a value of 1.

If:

$|\tau| \leq \tau_{max}$

then

$\tau' = \tau$

and Shear_Max will be given a value of 0.

• Step 3. Solve for several iterations until the solution is reasonably well converged (typically 500 after which the residuals which measure the stability of the solution flatten).
• Step 4. Continue iterating the solution while updating the wall shear stress according to:

a) Case 1. If Shear_Max = 1 and

$v_{relt} \leq 0$

The shear stress at the wall is limited by the maximum value and slip is occurring. In this case the wall shear stress is updated according to equation (A.11) and the procedure in section 2.

b) Case 2. If Shear_Max = 1 and

$v_{relt} > 0$

The shear stress at the wall is limited by the maximum value from the previous step. However the shear stress is such that the material at this position is actually moving faster than the tool which is clearly impossible. Therefore it is necessary to change the boundary condition so that the maximum shear stress is no longer defined, i.e. set Shear_Max = 0 and go to Case 3.

c) Case 3. If Shear_Max = 0, then the material is stuck to the tool and the shear stress needs to be updated according to:

$$\tau' = \tau + C\,\mathbf{v_{rel}} \tag{A.13}$$

where C is a constant. If C is too large the system will go unstable, and if too small the system will take a long time to solve. $\mathbf{v_{rel}}$ is given by equation (A.4). Suitable values were found by trial-and-error.

This equation forces the value of $\mathbf{v_{rel}}$ to converge on zero, by adjusting the wall shear stress based on the value of this slip velocity. Where the new value of the shear stress exceeds the maximum allowable, i.e.

$|\tau'| > \tau_{max}$

then a slip boundary condition is applied by allowing Shear_Max = 1. The shear stress is set by:

$$\tau' = \tau_{max}\frac{\tau}{|\tau|} \tag{A.14}$$

i.e. the limiting shear stress is applied in the direction of the existing shear stress.

APPENDIX B: LOGIC FOR ADJUSTING THE LIMITING SHEAR STRESS FOR THE TORQUE CALIBRATED MODELS

This appendix describes how the limiting shear stress, τ_{max} was adjusted so that the torque (and hence power input) to the weld matched the actual weld torque (and power input). The steps used by the model were:
• Step 1. Find the torque, T_a which is being applied to the surface due to the limiting shear stress τ_{max}.
• Step 2. Find the new value of the limiting shear stress, τ_{max} from the following equation:

$$\tau_{max}' = \tau_{max} + (T_{set} - T_a)\,C_3\,\frac{\tau_{max}}{T_a} \tag{B.1}$$

where:

T_{set} = The required torque.

C_3 = update constant.

Note that the change in the value is dependent on the ratio of $\frac{\tau_{max}}{T_a}$

• Step 3. Iterate for 50 iterations so that the solutions stabilises for the new value of τ_{max}, then repeat Step 1.